

Bayesian inference of ocean diffusivity from Lagrangian trajectory data

Y.K. Ying*, J.R. Maddison, J. Vanneste

School of Mathematics and Maxwell Institute for Mathematical Sciences, The University of Edinburgh, Edinburgh EH9 3FD, United Kingdom



ARTICLE INFO

Article history:

Received 12 December 2018

Received in revised form 8 May 2019

Accepted 12 June 2019

Available online 25 June 2019

Keywords:

Bayesian inference

Lagrangian particles

Ocean diffusivity

Stochastic differential equations

Markov Chain Monte Carlo

ABSTRACT

A Bayesian approach is developed for the inference of an eddy-diffusivity field from Lagrangian trajectory data. The motion of Lagrangian particles is modelled by a stochastic differential equation associated with the advection-diffusion equation. An inference scheme is constructed for the unknown parameters that appear in this equation, namely the mean velocity, velocity gradient, and diffusivity tensor. The scheme provides a posterior probability distribution for these parameters, which is sampled using the Metropolis-Hastings algorithm. The approach is applied first to a simple periodic flow, for which the results are compared with the prediction from homogenisation theory, and then to trajectories in a three-layer quasigeostrophic double-gyre simulation. The statistics of the inferred diffusivity tensor are examined for varying sampling interval and compared with a standard diagnostic of ocean diffusivity. The Bayesian approach proves capable of estimating spatially-variable anisotropic diffusivity fields from a relatively modest amount of data while providing a measure of the uncertainty of the estimates.

© 2019 Published by Elsevier Ltd.

1. Introduction

Turbulent processes can lead, on sufficiently long time scales, to diffusive mixing of tracer quantities (Taylor, 1922; Majda and Kramer, 1999). In the ocean large-scale instabilities gives rise to geostrophic eddies. These energetic eddies dominate the redistribution of heat and tracers both laterally and vertically (e.g. Jayne and Marotzke, 2002) and contribute to the formation of large-scale circulation patterns (e.g. Marshall and Radko, 2003; Hallberg and Gnanadesikan, 2006). The mixing induced by these eddies is typically modelled through an “eddy diffusivity”. Diffusive models can be shown to be valid in limiting cases (e.g. Davis, 1987; Majda and Kramer, 1999), although the empirically long (~ 100 days) time for the diffusive regime to come into effect in some parts of the ocean (Rypina et al., 2012) makes their general applicability questionable.

There are multiple approaches for the diagnosis of turbulent ocean eddy diffusivities, which are not obviously equivalent. One can diagnose a diffusivity from turbulent eddy fluxes (e.g. Bachman and Fox-Kemper, 2013), although this may be prone to ambiguity due to the possible presence of rotational fluxes (Marshall and Shutts, 1981). Alternatively, observations of the motion of tracer contours can be used to define an eddy diffusivity (Marshall et al., 2006; Nakamura, 1996). A separate broad class of diffusivity diagnostics is based upon observations of the motion of fluid parcels

(e.g. LaCasce, 2008; van Sebille et al., 2018), which may for example be obtained from simulated Lagrangian trajectories, or from ocean drifter data. For comparisons between these approaches see Klocker et al. (2012) and Abernathay et al. (2013).

Consider Lagrangian particles, where the i th particle has position $\mathbf{X}_i(t)$ and corresponding displacement $\mathbf{S}_i(t) = \mathbf{X}_i(t) - \mathbf{X}_i(0)$. In a statistically stationary and homogeneous flow one may define an absolute diffusivity tensor K_{abs} based upon the absolute dispersion of particles (Taylor, 1922; LaCasce, 2008)

$$K_{abs}(\tau) = \frac{1}{2} \frac{d}{d\tau} \langle \mathbf{S}_i(\tau) \otimes \mathbf{S}_i(\tau) \rangle, \quad (1)$$

where \otimes is the outer product, $\langle \cdot \rangle$ denotes an appropriate average over particles, such as an ensemble average, and τ represents a time window over which the particle trajectories are considered. As $\tau \rightarrow \infty$, $K_{abs}(\tau)$ converges to a constant and characterises the asymptotic growth rate of particle dispersion. This definition makes no correction for the possible presence of a background mean flow, which can for example be accounted for via

$$K_{abs}(\tau) = \frac{1}{2} \frac{d}{d\tau} \langle (\mathbf{S}_i(\tau) - \langle \mathbf{S}_i(\tau) \rangle) \otimes (\mathbf{S}_i(\tau) - \langle \mathbf{S}_i(\tau) \rangle) \rangle, \quad (2)$$

correcting for a mean drift (e.g. Sallée et al., 2008).

* Corresponding author.

E-mail address: Y.K.Ying@ed.ac.uk (Y.K. Ying).

Retaining the assumption of a statistically stationary and homogeneous flow, one may define a relative diffusivity (e.g. LaCasce, 2008)

$$\kappa_{\text{rel}}(\tau) = \frac{1}{4} \frac{d}{d\tau} \langle (\mathbf{X}_{i_1}(\tau) - \mathbf{X}_{i_2}(\tau)) \otimes (\mathbf{X}_{i_1}(\tau) - \mathbf{X}_{i_2}(\tau)) \rangle, \quad (3)$$

where now the average is taken over all distinct pairs of particles ($i_1 \neq i_2$). This automatically takes account of the presence of a uniform background mean flow. Such a relative diffusivity has been used to study energy spectra in fluid turbulence (e.g. Koszalka et al., 2009; Lumpkin and Eliot, 2010).

The above definitions make use of statistical homogeneity to yield a single bulk uniform diffusivity. This is problematic if the diffusivity is expected to vary in different regions of the ocean. To account for this, Davis (1987, 1991) defines the spatially dependent diffusivity

$$\kappa_{\text{Davis}}(\mathbf{x}; \tau) = \int_{-\tau}^0 \left\langle \left[\dot{\mathbf{X}}_i(t) - \bar{\mathbf{u}}(\mathbf{x}) \right] \otimes \left[\dot{\mathbf{X}}_i(t+s) - \bar{\mathbf{u}}(\mathbf{X}_i(t+s)) \right] \right\rangle_{\{\mathbf{X}_i(t)=\mathbf{x}\}} ds, \quad (4)$$

where the conditional average $\langle \cdot \rangle_{\{\mathbf{X}_i(t)=\mathbf{x}\}}$ is taken over all trajectories $\mathbf{X}_i(t)$ that pass through position \mathbf{x} at some time t . While this definition captures spatial variations in diffusivity, it requires the choice of an appropriate background mean flow $\bar{\mathbf{u}}(\mathbf{x})$. Its implementation is further complicated by the need for past history information of particles which arrive at a common point – in practice this necessitates local binning of particles which arrive in the vicinity of a point, and may also be replaced with future information of particles which leave the vicinity (e.g. Oh et al., 2000; Griesel et al., 2010; Klocker et al., 2012; Rühs et al., 2018).

A concern in the Davis (1987) diffusivity is its dependence on the time-lag parameter τ . One may hope for convergence in the large- τ limit, after some characteristic decorrelation time, but this decorrelation time may be sufficiently large that the particles have left the neighbourhood of \mathbf{x} . As a result, particles involved in the calculation experience different flow regions, with different diffusivity properties, over the timescale τ over which the integral is taken. These non-local effects mean that care needs to be exercised when interpreting the spatial dependence of the Davis (1987) diffusivity. Further, there is the concern that in general this diffusivity need not be non-negative definite, nor even symmetric.

In this article we present a new approach for the diagnosis of ocean eddy diffusivity from Lagrangian particle data using Bayesian inference. Given a stochastic model for the particle motion, discretely observed Lagrangian particle positions, and prior information, the approach infers a joint posterior probability distribution for both a local flow velocity and a local anisotropic diffusivity tensor. This probability distribution makes it possible, for example, to compute mean quantities or to find maximum a posteriori estimates, and to quantify the uncertainty of these estimates. In common with other Lagrangian diffusivity diagnostics, the approach is dependent on the validity of the underlying diffusive model and, in the implementation discussed, uses an assumption of locality similar to that of the Davis (1987) diffusivity.

The paper is organised as follows. In Section 2 the Bayesian inference approach and its implementation using Monte Carlo Markov Chain are described. Section 3 provides an application in an idealised configuration. In Section 4 the approach is applied to Lagrangian particle data obtained from a three-layer quasigeostrophic double-gyre calculation, and the resulting diffusivity diagnosis is compared against the Davis (1987) diffusivity. The paper concludes in Section 5 with an outlook towards more general applications of Bayesian inference to the analysis of Lagrangian drifter data.

2. Mathematical background

2.1. Stochastic Lagrangian particle dynamics

The position $\mathbf{X}(t)$ of particles advected in a time-dependent velocity field $\mathbf{u}(\mathbf{x}, t)$ satisfies the ordinary differential equation

$$\frac{d\mathbf{X}}{dt} = \mathbf{u}(\mathbf{X}(t), t), \quad (5)$$

subject to some initial condition $\mathbf{X}(0) = \mathbf{x}_0$. The concept of eddy diffusivity arises when attempting to coarse-grain this equation: it might be expected that over sufficiently long time scales the behaviour of its solutions is well captured by the stochastic differential equation (SDE)

$$d\mathbf{X} = [\mathbf{U}(\mathbf{X}(t)) + \nabla \cdot \mathbf{K}(\mathbf{X}(t))] dt + \sqrt{2 \kappa(\mathbf{X}(t))} d\mathbf{W}, \quad (6)$$

termed Markov-0 model by Berloff and McWilliams (2002). Now \mathbf{U} is a time-independent coarse-grained average velocity field, \mathbf{K} is the eddy diffusivity which is a symmetric positive definite tensor (whose square root is uniquely defined by requiring that it too be symmetric positive definite), and \mathbf{W} is multi-dimensional Brownian motion. The reduction from Eq. (5) to the Markov-0 model (6) can only be justified rigorously, and explicit expressions for \mathbf{U} and \mathbf{K} can only be obtained, when $\mathbf{u}(\mathbf{x}, t)$ satisfies strong assumptions of scale separation in time and/or space that are not met in the context of the ocean (see Griffa, 1996, and references therein). Here we adopt a heuristic approach and seek to estimate values for \mathbf{U} and \mathbf{K} that are most consistent – in a sense to be explained – with a set of observed particle trajectories $\mathbf{X}_i(t)$.

The evolution of $\mathbf{X}(t)$ according to Eq. (6) is entirely characterised by the transition probability density $\pi(\mathbf{x}, t | \mathbf{x}_0)$ which defines the probability of finding the particle in the neighbourhood of \mathbf{x} at time t given it is initially at \mathbf{x}_0 . The transition probability evolves under the Fokker–Planck equation (e.g. Evans, 2013; Pavlitos, 2014)

$$\frac{\partial \pi}{\partial t} + \nabla \cdot (\mathbf{U} \pi) = \nabla \cdot (\mathbf{K} \nabla \pi), \quad (7)$$

with initial condition $\pi(\mathbf{x}, 0 | \mathbf{x}_0) = \delta(\mathbf{x} - \mathbf{x}_0)$. This is the advection-diffusion equation, and hence Eq. (6) is a natural stochastic model for advective and diffusive processes.

The velocity and diffusivity fields \mathbf{U} and \mathbf{K} are fields defined over the entire spatial domain. For practical computations it is necessary to first discretise these fields over space,

$$\mathbf{U}(\mathbf{x}) = \mathbf{U}(\mathbf{x}; \boldsymbol{\theta}) \quad \text{and} \quad \mathbf{K}(\mathbf{x}) = \mathbf{K}(\mathbf{x}; \boldsymbol{\theta}), \quad (8)$$

where $\boldsymbol{\theta}$ denotes the degrees of freedom for both \mathbf{U} and \mathbf{K} – that is, $\boldsymbol{\theta}$ is a finite-length vector of parameters which specifies the discrete approximation for \mathbf{U} and \mathbf{K} . Hereafter the dependence of quantities on $\boldsymbol{\theta}$ is omitted, but it should be borne in mind that most objects of interest, the transition probability π for instance, have such a dependence. The problem of estimating the discretised velocity and diffusivity fields now reduces to the estimation of $\boldsymbol{\theta}$. In the Bayesian-inference approach we adopt, $\boldsymbol{\theta}$ is regarded as a random variable and its entire probability distribution, and hence a probability distribution for (\mathbf{U}, \mathbf{K}) , is estimated from trajectory data.

2.2. Bayesian inference

Given N particles each observed at P distinct times t_j , evolving under the SDE (6), Bayes' theorem gives (a thorough textbook

reference for Bayesian statistics is Gelman et al., 2013)

$$p(\boldsymbol{\theta}|R) = \frac{p(R|\boldsymbol{\theta}) p(\boldsymbol{\theta})}{\int p(R|\boldsymbol{\theta}) p(\boldsymbol{\theta}) d\boldsymbol{\theta}} \propto p(R|\boldsymbol{\theta}) p(\boldsymbol{\theta}), \quad (9)$$

where the integral is over the full parameter space. R denotes the data, and can be set equal to the full trajectory,

$$R = \{(i, \mathbf{X}_i(t_j), t_j) : i = 1, \dots, N, j = 1, \dots, P\}, \quad (10)$$

where $\mathbf{X}_i(t_j)$ is the position of the i th particle at the j th observation time. Equivalently, as the SDE is Markovian, R can be replaced with

$$R = \{(\mathbf{X}_i(t_j), \mathbf{X}_i(t_{j+1}), t_{j+1} - t_j) : i = 1, \dots, N, j = 1, \dots, P-1\}. \quad (11)$$

That is, the data consist of the start and end positions of each particle between consecutive pairs of observations, and the time separation between the observations. Note that this is easily generalised for the case of differing observation times for each particle and differing particle trajectory lengths.

Three key probability distributions appear in Eq. (9): the posterior $p(\boldsymbol{\theta}|R)$, the likelihood $p(R|\boldsymbol{\theta})$, and the prior $p(\boldsymbol{\theta})$. The posterior $p(\boldsymbol{\theta}|R)$ is the probability distribution of the parameter $\boldsymbol{\theta}$ given the observations and the model, and its determination is the goal of the inference. It should be interpreted as an objective measure of the plausibility of a certain value of $\boldsymbol{\theta}$ (and hence of \mathbf{U} and K) in view of the observations, assuming the model is perfect. The likelihood $p(R|\boldsymbol{\theta})$ is the probability that particles evolving according to Eq. (6), and with (\mathbf{U}, K) fixed by $\boldsymbol{\theta}$, have positions matching R . It is given explicitly in terms of a product of transition probabilities

$$p(R|\boldsymbol{\theta}) = \prod_{i=1}^N \prod_{j=1}^{P-1} \pi(\mathbf{X}_i(t_{j+1}), t_{j+1} - t_j | \mathbf{X}_i(t_j)). \quad (12)$$

The prior $p(\boldsymbol{\theta})$ is a subjective choice for the plausibility of a given set of parameters $\boldsymbol{\theta}$ in the absence of data. Its relative importance for the posterior is expected to diminish as the number $N(P-1)$ of data points increases. We note that the number of data points can be increased by deploying more drifters or lengthening the duration of observation; both would have an identical effect on the posterior.

2.3. Sampling: Metropolis–Hastings

Assuming we can evaluate the transition probability in Eq. (12), Bayes' formula (9) gives the probability density for the parameters $\boldsymbol{\theta}$ and therefore for \mathbf{U} and K in an explicit form. This is however a probability density in a high-dimensional space which cannot be visualised and from which derived quantities cannot be computed directly. Instead, one is interested in computing integrals of various quantities against the posterior – that is, in evaluating

$$\int f(\boldsymbol{\theta}) p(\boldsymbol{\theta}|R) d\boldsymbol{\theta} \quad (13)$$

for some $f(\boldsymbol{\theta})$. For example $f(\boldsymbol{\theta}) = K$ yields the posterior mean diffusivity, \bar{K} say, which can be used as an estimate for the eddy diffusivity, while $f(\boldsymbol{\theta}) = \|K - \bar{K}\|^2$ yields a variance characterising the uncertainty of the estimate \bar{K} .

Markov Chain Monte Carlo (MCMC) methods can be used to obtain numerical approximations for integrals of the form (13). These methods generate sequences of random samples $\boldsymbol{\theta}^{(k)}$ using a transition probability $T(\boldsymbol{\theta}^{(k+1)}|\boldsymbol{\theta}^{(k)})$ chosen to ensure that, for large k , the $\boldsymbol{\theta}^{(k)}$ are distributed according to $p(\boldsymbol{\theta}|R)$. The integrals (13) are

then estimated simply by the arithmetic mean of $f(\boldsymbol{\theta}^{(k)})$. Here we use the well-known Metropolis–Hastings algorithm, based on an acceptance/rejection definition of $T(\boldsymbol{\theta}^{(k+1)}|\boldsymbol{\theta}^{(k)})$, and more specifically the Gibbs sampler (e.g. Geman and Geman, 1984) for which the successive samples $\boldsymbol{\theta}^{(k)}$ and $\boldsymbol{\theta}^{(k+1)}$ differ in at most one component. The reliable estimation of integrals using MCMC requires monitoring the convergence of the estimates and ensuring that the $\boldsymbol{\theta}^{(k)}$ properly explore the support of $p(\boldsymbol{\theta}|R)$; we adopt the Gelman and Rubin (1992) diagnostic (also in Appendix A and in Section 11.4 of Gelman et al., 2013) to verify this.

2.4. Local inference

The specific inference problem considered in this article is conducted in a local cell-wise manner. The domain of interest is partitioned into a coarse mesh, and we seek to obtain information on the flow velocity and diffusivity for each mesh cell. The result of the inference is expected to be dependent on the choice of mesh, and in particular on the mesh cell size. This is consistent with the coarse graining involved in approximating Eq. (5) by Eq. (6) – the eddy diffusivity obtained is dependent upon the spatial scales.

Note that a meaningful eddy diffusivity is only realised after a decorrelation time scale. Over short time scales, correlated advection associated with the so-called “ballistic” regime (e.g. Pasquero et al., 2007; Rypina et al., 2012) dominates and is incompatible with the diffusive model (6). It is therefore necessary to ensure that the pairs of observed particle positions employed are separated by a sufficient time interval – a principle noted in a multi-scale system in Pavlitos and Stuart (2007) (see also Cotter and Pavlitos, 2009, for an application to eddy diffusivity). An optimal sampling interval, which discards the minimum number of position records while preserving the validity of the model (6), is rarely known a priori. In practice the inference is performed with varying sampling intervals and the convergence of the various estimates is examined. In the local inference approach we take here it is also necessary for the particles to remain in (or at least close to) the cell considered over the sampling interval. There is therefore a trade-off between two competing requirements: the sampling interval must be long enough that the particles do decorrelate, and short enough that they are not transported far from the considered cell. One must therefore take care to choose an appropriate sampling interval between observations, and be aware that this may not always exist. The possibility for a more advanced “non-local” inference, which alleviates this difficulty, is discussed in the conclusions.

3. Idealised example: Taylor–Green vortices with a background flow

3.1. Configuration

A highly idealised model of oceanic eddies in a background current is constructed by superimposing a constant mean flow on top of Taylor–Green vortices, leading to the two-dimensional and doubly-periodic steady velocity field

$$\mathbf{u}(\mathbf{x}) = u_{TG} \begin{pmatrix} -\sin(2\pi x/l) \cos(2\pi y/l) \\ \cos(2\pi x/l) \sin(2\pi y/l) \end{pmatrix} + u_M \begin{pmatrix} \cos \phi_M \\ \sin \phi_M \end{pmatrix}, \quad (14)$$

where u_{TG} is the maximum vortex speed, u_M is a background flow speed, and ϕ_M is the angle of the background flow to the x -axis. The small-scale advection–diffusion of particles according to

$$d\mathbf{X} = \mathbf{u}(\mathbf{X}(t)) dt + \sqrt{2\kappa} d\mathbf{W}, \quad (15)$$

Table 1

Parameters used in the idealised Taylor–Green vortex configuration.

Parameter	Symbol	Value(s)
Spatial period	l	100 km
Maximum vortex speed	u_{TG}	40 cm s ⁻¹
Background flow speed	u_M	20 cm s ⁻¹
Background flow angle	ϕ_M	30°
Small-scale diffusivity	κ	50 m ² s ⁻¹
Particle integration timestep size	–	84.3750 s
Total particle integration time	–	256 days
Number of particles	–	256
Data sampling interval	s	3 h, 6 h, ..., 120 days
Markov Chain Monte Carlo iterations	N_{mh}	10 ⁵
Number of independent Markov Chains	M	3

is considered, where $\kappa \neq 0$ is here a small-scale scalar diffusivity. Note that κ , which governs the small-scale motion of the particles, is not the object to be inferred in this problem. Rather we seek to infer information about a large-scale effective diffusivity, which governs the long-time behaviour.

Homogenisation theory (e.g. Majda and Kramer, 1999; Majda and McLaughlin, 1993) provides rigorous coarse-graining results for this problem. Specifically, over scales much larger than the vortex period l , the motion of particles is approximated by the SDE (6) with a uniform mean velocity $\mathbf{U} = u_M(\cos \phi_M, \sin \phi_M)^T$ and an effective diffusivity tensor K . The effective diffusivity tensor K can be computed by solving a two-dimensional elliptic problem known as the “cell problem” (e.g. Pavliotis and Stuart, 2008).¹

3.2. Bayesian inference

We apply Bayesian inference to this problem for the uniform velocity and diffusivity

$$\mathbf{U} = \mathbf{U}(\boldsymbol{\theta}) = U_0 \begin{pmatrix} \cos \Phi_0 \\ \sin \Phi_0 \end{pmatrix}, \quad (16a)$$

$$K = K(\boldsymbol{\theta}) = R(\Phi_K) \begin{pmatrix} \Gamma_1 & 0 \\ 0 & \Gamma_2 \end{pmatrix} R(\Phi_K)^T, \quad (16b)$$

where

$$R(\Phi_K) = \begin{pmatrix} \cos \Phi_K & -\sin \Phi_K \\ \sin \Phi_K & \cos \Phi_K \end{pmatrix} \quad (17)$$

is a rotation matrix. Thus the parameters to infer are

$$\boldsymbol{\theta} = (U_0, \Phi_0, \Gamma_1, \Gamma_2, \Phi_K)^T. \quad (18)$$

The representation (16b) of the diffusivity K is motivated by its eigendecomposition, and guarantees that it is symmetric positive-definite when the eigenvalues Γ_1 and Γ_2 are positive, regardless of the orientation Φ_K of the eigenvector associated with Γ_1 .

Parameters used in this example are provided in Table 1. The domain size, flow speeds, and small-scale diffusivity are chosen so as to yield an ocean-like regime. Particle trajectory data are generated by solving the SDE (15) for 256 particles initially located on a uniform square grid in the doubly-periodic domain $(x, y) \in [-l, l]^2$. The SDE is solved numerically using the Euler–Maruyama method with a small timestep size of 84.3750 s. For the purposes of the Bayesian inference their positions are sampled with a sampling interval $s = t_j - t_{j-1}$ over a total time of 256 days.

3.3. Posterior evaluation

For the uniform velocity and diffusivity (16), the Fokker–Planck equation can be solved analytically (see Appendix D.3), yielding the Gaussian transition probability density

$$\pi(\mathbf{X}_i(t_{j+1}), s | \mathbf{X}_i(t_j)) = \frac{1}{2\pi\sqrt{\det \Sigma_s}} \exp\left(-\frac{1}{2} \|\mathbf{X}_i(t_{j+1}) - \mathbf{m}_s(\mathbf{X}_i(t_j))\|_{\Sigma_s^{-1}}^2\right), \quad (19)$$

where

$$\mathbf{m}_s(\mathbf{x}) = \mathbf{x} + \mathbf{Us}, \quad \Sigma_s = 2sK \quad (20)$$

and, for a suitably sized vector \mathbf{v} , the square norm $\|\mathbf{v}\|_{\Sigma_s^{-1}}^2$ is defined to be

$$\|\mathbf{v}\|_{\Sigma_s^{-1}}^2 = \mathbf{v}^T \Sigma_s^{-1} \mathbf{v}. \quad (21)$$

This gives an explicit expression for the likelihood (12).

In order to perform the Bayesian inference a prior must be chosen. This is a subjective choice reflecting expected prior knowledge regarding the parameters under consideration (the elements of $\boldsymbol{\theta}$) and, except in limiting cases of large data, the result of the inference is dependent upon the choice of prior. In the absence of strong constraints, the priors for the angles Φ_0 and Φ_K are set equal to the uniform distribution and priors for the remaining parameters are uniform in the ranges $U_0 \in [0, 10 \text{ m s}^{-1}]$ and $\Gamma_1, \Gamma_2 \in [1 \text{ m}^2 \text{ s}^{-1}, 10^5 \text{ m}^2 \text{ s}^{-1}]$, and zero elsewhere. If more information was available about the problem, more restrictive priors could be chosen.

The posterior is evaluated, up to some unknown proportionality constant, as the product of the likelihood and the prior, noting that the proportionality constant is not required by the Metropolis–Hastings algorithm. In total 3 independent set of 100,000 samples $\boldsymbol{\theta}^{(k)}$ are drawn, and it is verified that the Gelman–Rubin diagnostic criterion (see Appendix A) is satisfied.

3.4. Results

The posterior mean velocity components (not shown) show little variability with sampling interval and agree excellently with the background flow. The posterior mean diffusivity components are shown in Fig. 1, and show much greater variability. For example, over short time scales the particles experience only local small-scale dynamics, and hence short sampling intervals are associated with low values of inferred diffusivity. The diffusivity components

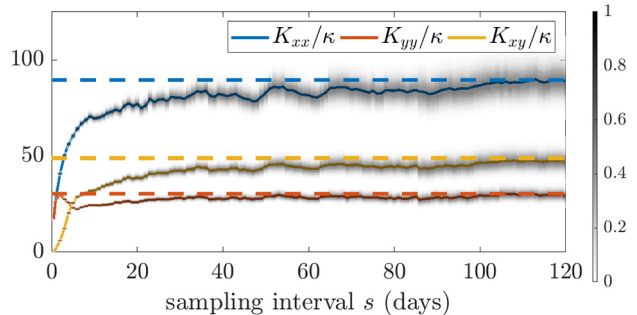


Fig. 1. Results of the Bayesian inference for the diffusivity tensor components for the periodic flow (14) under varying sampling intervals. The posterior distributions are shown with shading, normalised so that the maximum value at each sampling interval is 1. The posterior means are shown as solid lines. The computed effective diffusivity components of homogenisation theory are shown as dashed lines.

¹ Note that the “effective diffusivity” appearing here should not be confused with the “effective diffusivity” in Marshall et al. (2006).

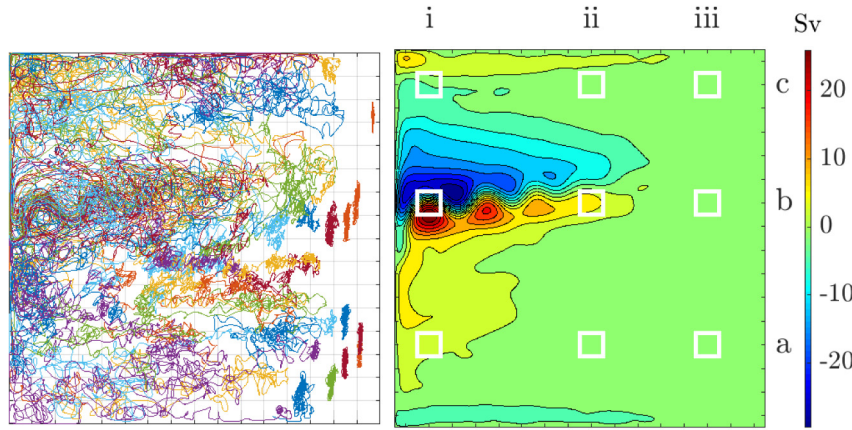


Fig. 2. Left panel: 10-year trajectories for 50 arbitrarily selected particles in the middle layer of the quasigeostrophic double-gyre system. The division of the domain into a 16×16 array of square elements is shown in grey. Right panel: 10-year time-averaged streamfunction, multiplied by the layer thickness, in the middle layer. Selected cells of the 16×16 array referred to in the main text are highlighted in white and labelled by a letter/numerical coordinate.

increase with increasing sampling interval and approach a stable value. As the sampling interval increases, the number of particle positions used in the inference decreases (since the same length of particle trajectory is considered in all cases). As a result, the uncertainty of the inference increases, leading to a widening of the posterior distribution.

For reference the effective diffusivity K of homogenisation theory is computed by solving the elliptic “cell problem” (e.g. Eq. (2.2) of Cotter and Pavloutis, 2009). The equations are solved using degree-one continuous Lagrange finite elements using the FEniCS system (Logg et al., 2012; Alnæs et al., 2015) version 2018.1.0. A finite element mesh is formed via a 512×512 structured and uniform square mesh, with each square divided along the lower-left to upper-right diagonal to form a triangle mesh. The results are shown with dashed lines in Fig. 1. The larger sampling interval posterior mean diffusivity components, obtained using Bayesian inference, agree well with the computed effective diffusivity.

4. Quasigeostrophic double gyre

The Bayesian inference machinery, illustrated in the preceding section for a highly idealised example, is now applied in a more oceanographically relevant context by considering Lagrangian particle trajectories in a quasigeostrophic double-gyre calculation.

4.1. Numerical model

The three-layer quasigeostrophic double gyre configuration of Maddison et al. (2015) is considered (see also Berloff et al., 2007; Karabasov et al., 2009; Marshall et al., 2012). The three-layer quasigeostrophic equations (see Appendix E and Maddison et al., 2015) are discretised using finite differencing, with a mesh with 513×513 nodes uniformly spaced on a square grid, in a $3840 \text{ km} \times 3840 \text{ km}$ square horizontal domain. The advection term in the quasigeostrophic potential vorticity equation is discretised using the Arakawa (1966) Jacobian, and Laplace operators are discretised using second order centred differencing. The elliptic problem for potential vorticity inversion is solved via projection onto discrete baroclinic modes, and the resulting Poisson or modified Helmholtz problems are solved using a Fast Poisson Solver (e.g. Strang, 1986, Section 5.5), with the decoupled tri-diagonal systems arrived at using a Discrete Sine Transform using FFTPACK 5.1. The system is integrated in time using a third-order Adams–Bashforth scheme with uniform timestep $\Delta t_{QC} = 1800 \text{ s}$. Physical parameters are given in Appendix E, and are as in Table 1 of Maddison et al. (2015).

4.2. Particle advection

Particles are advected using the geometric integration approach described in Ham et al. (2006) and Ham (2006). A piecewise linear streamfunction is constructed from the finite-difference grid point values by dividing each square cell corner-to-corner to yield four isosceles triangles, bi-linearly interpolating to yield a value at the centre vertex, and then linearly interpolating within the triangles. The time-dependent streamfunction is further linearly interpolated in time. Initial starting cells are determined using a quad-tree based search (Samet, 1984) using code derived from libsupermesh (Panourgiadis and Maddison, 2016), after which they are advected along contours of the discrete streamfunction. Note that care needs to be taken to ensure that the particle advection – which is a two-dimensional computational geometry problem – is solved in a precision-robust manner. A useful property of the particle advection scheme is that, given a streamfunction which is constant on the boundary, particles are guaranteed to never leave the bounding domain (see Ham et al., 2006). Hence the particle advection scheme requires no further consideration of boundary conditions.

We consider only particle advection, with no explicit small-scale diffusivity, within the middle layer of the model. This layer experiences no direct wind forcing or bottom linear drag. After a 100 year spinup² 676 particles are distributed uniformly across the square domain. This number is chosen so as to resemble the typical number of ARGO drifters available in the North Atlantic (Argo, 2000). The particles are then advected for a further 10 years, and their positions are recorded daily. The resulting trajectories for 50 arbitrarily selected particles are shown in Fig. 2.

4.3. Bayesian inference

The domain is partitioned into a 16×16 array of square cells with 240 km side lengths. Within each cell the velocity is represented as a linearly varying non-divergent field, and the diffusivity as a constant symmetric positive definite tensor,

$$\mathbf{U}(\mathbf{x}) = \mathbf{U}(\mathbf{x}; \boldsymbol{\theta}) = \mathbf{A}(\mathbf{x} - \mathbf{x}_0) + \mathbf{U}_0, \quad (22a)$$

$$\mathbf{K} = \mathbf{K}(\boldsymbol{\theta}) = \mathbf{R}(\Phi_K) \begin{pmatrix} \Gamma_1 & 0 \\ 0 & \Gamma_2 \end{pmatrix} \mathbf{R}(\Phi_K)^T, \quad (22b)$$

² Julian years are used throughout.

where

$$\mathbf{U}_0 = \mathbf{U}_0(\boldsymbol{\theta}) = U_0 \begin{pmatrix} \cos \Phi_0 \\ \sin \Phi_0 \end{pmatrix}, \quad (23a)$$

$$\mathbf{A} = \mathbf{A}(\boldsymbol{\theta}) = \mathbf{R}(\Phi_A) \begin{pmatrix} 0 & \Upsilon_2 + \Upsilon_1 \\ \Upsilon_2 - \Upsilon_1 & 0 \end{pmatrix} \mathbf{R}(\Phi_A)^T. \quad (23b)$$

Here \mathbf{R} is a rotation matrix as in Eq. (17) and \mathbf{x}_0 is the centre of the cell. Thus the parameters to infer in each cell are

$$\boldsymbol{\theta} = (U_0, \Phi_0, \Upsilon_1, \Upsilon_2, \Phi_A, \Gamma_1, \Gamma_2, \Phi_K)^T. \quad (24)$$

The parameters Υ_1 and Υ_2 are related to the vorticity and strain associated with the velocity gradient tensor \mathbf{A} , as explained in Appendix D.

The linear velocity field introduces additional degrees of freedom compared with the uniform velocity field used in Section 3. It is motivated by the large shears that are present in the jet region of the simulation and that can severely bias the inferred diffusivity if unresolved (Oh et al., 2000; Griesel et al., 2010). It should be noted that the cell-wise linear velocity field is only a local approximation to the coarse-grained mean flow. The validity of the approximation can be justified on a sufficiently short time-scale when dispersion of particles remains dominated by the linear components in the shear.

4.4. Posterior evaluation

The Fokker–Planck equation can be solved analytically for the velocity and diffusivity (22), yielding the Gaussian transition

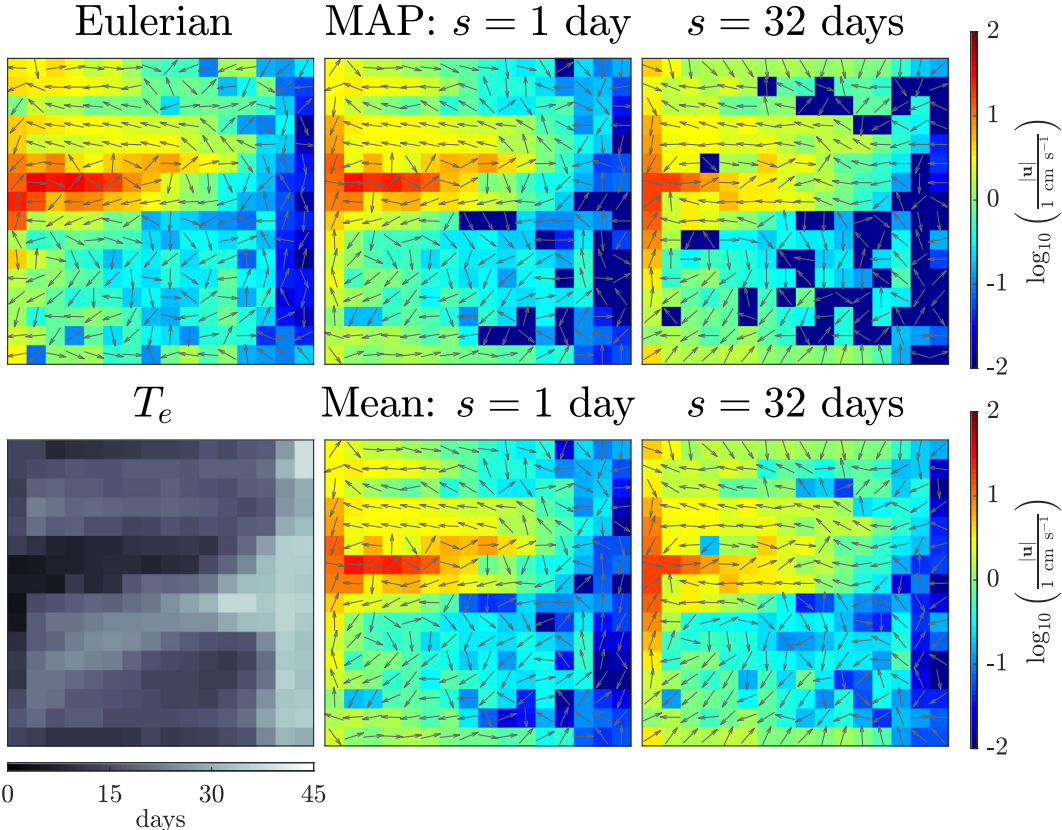


Fig. 3. Top left: 10-year Eulerian mean velocity in the middle layer at the cell centres. Top middle and right: Posterior mean for the cell-centre middle layer velocity using particle positions observed at sampling intervals of $s = 1$ day and $s = 32$ days. Bottom left: e -folding time T_e estimated from Lagrangian data. Bottom middle and right: Posterior mean for the cell-centre middle layer velocity using particle positions observed at sampling intervals of $s = 1$ day and $s = 32$ days. The magnitude of the velocity is shown using a logarithmic colour scale, and the velocity direction is indicated by equal-length arrows.

probability density

$$\pi(\mathbf{x}_i(t_{j+1}), s | \mathbf{x}_i(t_j)) = \frac{1}{2\pi\sqrt{\det \Sigma_s}} \exp\left(-\frac{1}{2} \|\mathbf{x}_i(t_{j+1}) - \mathbf{m}_s(\mathbf{x}_i(t_j))\|_{\Sigma_s^{-1}}^2\right), \quad (25)$$

where

$$\mathbf{m}_s(\mathbf{x}) = \mathbf{m}_s(\mathbf{x}; \boldsymbol{\theta}) = e^{\mathbf{A}s} \mathbf{x} + \int_0^s e^{\mathbf{A}t} dt (\mathbf{U}_0 - \mathbf{A}\mathbf{x}_0), \quad (26a)$$

$$\Sigma_s = \Sigma_s(\boldsymbol{\theta}) = 2 \int_0^s e^{\mathbf{A}t} \mathbf{K} e^{\mathbf{A}^T t} dt, \quad (26b)$$

and $\|\mathbf{v}\|_{\Sigma_s^{-1}}$ is defined in Eq. (21) (see Appendix D.3). This gives an explicit expression for the likelihood (12).

We take again simple uniform priors for $p(\boldsymbol{\theta})$: the angles Φ_0 , Φ_A , and Φ_K are uniform, and remaining parameters are uniformly distributed in the ranges $U_0 \in [0, 10 \text{ m s}^{-1}]$, $\Upsilon_1, \Upsilon_2 \in [-10^{-5} \text{ s}^{-1}, 10^{-5} \text{ s}^{-1}]$, $\Gamma_1, \Gamma_2 \in [1 \text{ m}^2 \text{ s}^{-1}, 10^5 \text{ m}^2 \text{ s}^{-1}]$ and are zero elsewhere. It has been verified that the results would be unaffected if these ranges were extended. The results would of course be affected were much more restrictive priors imposed.

The posterior is evaluated, up to some unknown proportionality constant, as the product of the likelihood and the prior. In total 10 independent chains of 4×10^5 samples $\boldsymbol{\theta}^{(k)}$ are then drawn using the Metropolis–Hastings algorithm and the Gelman and Rubin (1992) diagnostic (also in Appendix A and Section 11.4 of Gelman et al., 2013) to test convergence. This process is performed separately for each cell of the model domain. We consider the sampling intervals

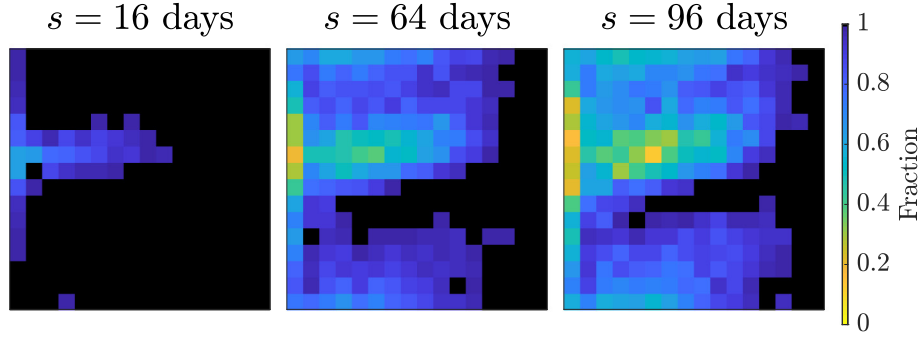


Fig. 4. Fractions of particles found in their origin cell, or in the eight cells surrounding the origin cell, at the end of the sampling interval. For sampling intervals shorter than 4 days all particles remain in this neighbourhood.

$s = 1, 2, 4, 8, 16, 24, 32, \dots, 128$ days. The samples of each of the independent chains are combined to approximate the posterior distribution.

4.5. Results

The upper middle and right panels of Fig. 3 show the maximum a posteriori estimate (MAP) for the middle-layer velocity field, together with the Eulerian mean flow computed over the 10-year data collection window on the left. The MAP estimate of θ is the maximiser for the posterior $p(\theta|R)$ and indicates the most likely combination of mean flow and diffusivity fields to recover the trajectory data. In all cases described here the MAP estimate is approximated by the sample $\theta^{(k)}$ that maximises the posterior $p(\theta^{(k)}|R)$ over all MCMC steps k and over all chains. For a short sampling interval $s = 1$ day, the MAP flow velocity is comparable to the Eulerian mean velocity. Over longer sampling intervals, where Lagrangian-mean effects are expected to play an increasing role, the inferred flow deviates from the Eulerian mean. The presence of local noise in the MAP estimate is attributed to multi-modal marginal distributions for mean flow magnitude in some cells. Note that the posterior mean velocity at cell centres, computed as a mean over all samples and shown in the bottom panels of Fig. 3, has a smoother profile.

The bottom left panel of Fig. 3 shows a Lagrangian eddy decorrelation time, specifically the e -folding scale T_e introduced by Garraffo et al. (2001) (see Appendix C). This is computed using 10,000 particle trajectories over the same 10-year period. The figure indicates that typical decorrelation time scales are of the order of about 10 days.

Fig. 4 shows the fraction of particles which are found in their cell of origin or in one of the eight surrounding cells at the end of sampling interval (regardless of the intermediate trajectory). This provides an indication of the validity of the locality assumption

inherent in the local inference approach. For short sampling intervals this fraction is high, but, as expected, drops as the sampling interval increases; in particular, it drops to very low values in the jet and on the western boundary. There is therefore potential misattribution of the spatial location of flow properties in these regions. This is a significant issue on the western boundary, where particles flow rapidly from the boundary into the jet, and rapidly change direction from a northward or southward flow, to an eastward flow.

At short sampling intervals ($\lesssim 16$ days), strong shears are inferred along the jet and on the northern, western, and southern boundaries. This is indicated by the large local vorticity $\omega = \partial_x v - \partial_y u$, corresponding to the off-diagonal elements of $A - A^T$, shown in Fig. 5. The inferred diffusivity in these areas is significantly reduced (not shown) when the spatial gradients of the mean flow are resolved, by permitting a non-zero linear shear. For the large sampling intervals the inferred shear tensor is smaller, as may be expected for a Lagrangian average of the flow over these time scales. Hence for the large sampling intervals the inferred diffusivity is largely unaffected by the inclusion of shear in $\mathbf{U}(\mathbf{x}; \theta)$, and an inference with a locally constant velocity would yield similar results.

Fig. 6 visualises the MAP estimate for the middle layer diffusivity tensor for differing sampling intervals. The “diffusivity ellipses” in Fig. 6 outline the orientations of contours of a passive tracer if it undergoes pure diffusion with a Dirac-delta initial profile, characterising the directions of the anisotropy of the eddy diffusion tensor. The diffusivity magnitude, defined as the half trace of the diffusivity tensor, is visualised using the colour scale. The inferred diffusivity is largest in the jet region, and strengthens with increasing sampling interval. There is a region of very weak inferred diffusivity in the eastern part of the southern half of the domain. At large sampling interval the anisotropic diffusion has a preferential east-west orientation in the gyres and the core of the jet. Near the western boundary the anisotropic diffusivity is tilted towards the direction of the jet – this

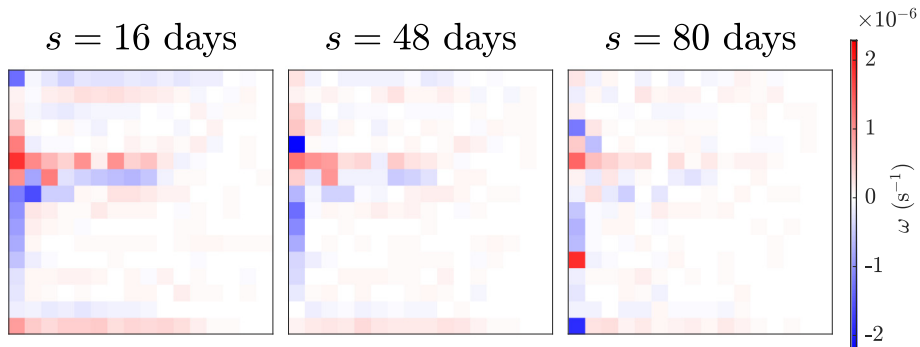


Fig. 5. MAP estimate of the vorticity $\omega = \partial_x v - \partial_y u$ field at different sampling intervals s .

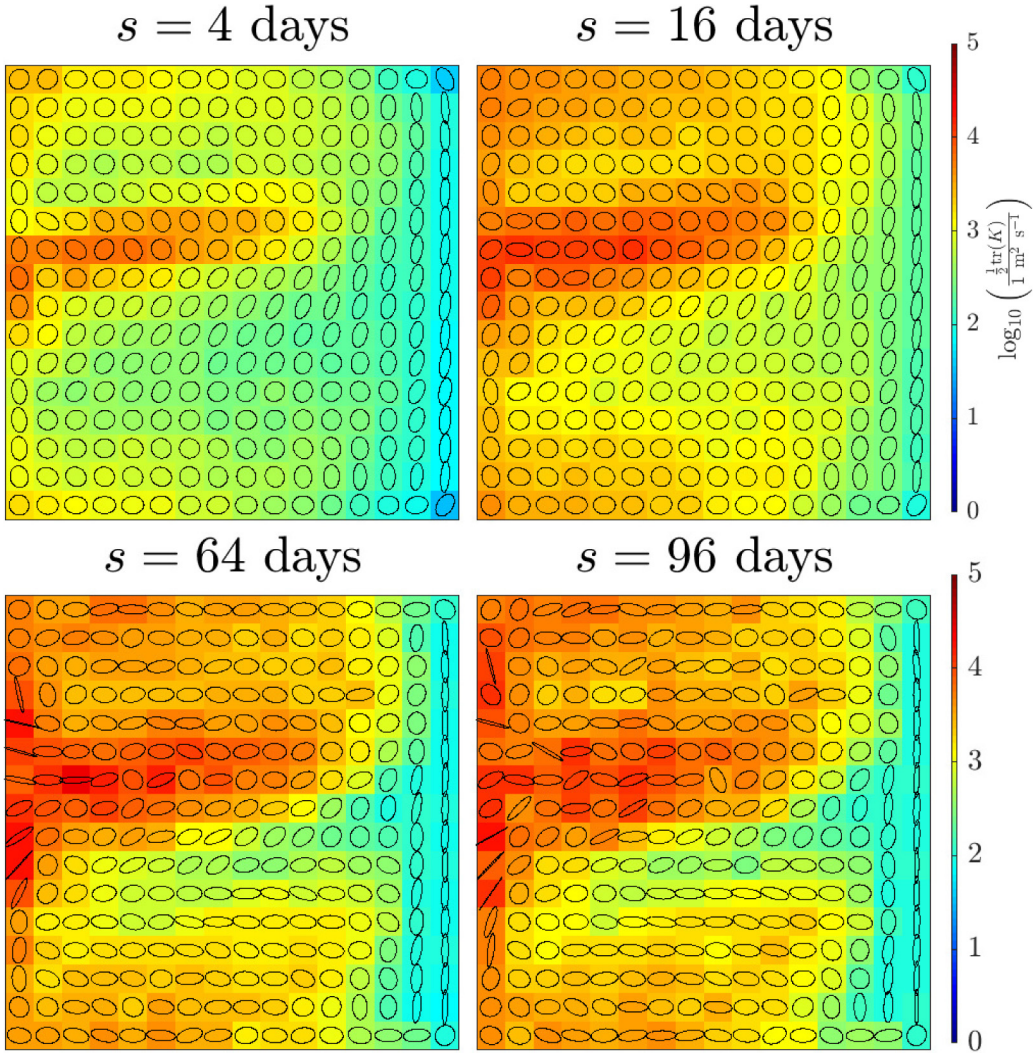


Fig. 6. MAP estimate of the middle layer diffusivity field at different sampling intervals s . The (logarithmic) colour scale gives the half trace of the diffusivity tensor K , which is also the arithmetic mean of the eigenvalues, to characterise the magnitude of diffusivity. The ellipses visualise the directions and the relative magnitude of the two eigenvectors of the diffusivity tensor in each cell.

is attributed to non-local effects, as particles are rapidly transported into the jet from this region.

The Metropolis–Hastings algorithm samples the joint posterior distribution of the velocity and diffusivity and so makes it possible to infer quantities that depend on both fields. In particular, we can construct distributions for the cross-stream and along-stream diffusivity components K^\perp and K^\parallel by projecting for each sample k , the sample diffusivity $K^{(k)}$, in directions perpendicular to and parallel to the sample velocity $\mathbf{U}^{(k)}$. The resulting MAP estimates are shown in Fig. 7. For comparison, the cross-stream and along-stream Davis (1987) diffusivity, defined with respect to the 10 year Eulerian mean flow at the cell centre, are shown in Fig. 8.

The two diagnostic approaches generally agree well in order of magnitude and spatial structure, with increased diffusivity in the region of the jet and reduced diffusivity on the eastern boundary and in the region south of the jet, as indicated by their relative differences in Fig. 9. There is some disagreement in detail, for example near the northern and southern boundaries. Note that the Davis (1987) diffusivity as computed here is not a symmetric positive definite (or even symmetric) quantity in general, leading to some regions of missing data indicated in white in Figs. 8 and 9.

To analyse our results in more detail, we now focus on the 9 cells highlighted in Fig. 2 and labelled (i)–(iii) with increasing x coordinate, and (a)–(c) with increasing y coordinate. Figs. 10 and 11 show the MAP of the middle layer cross-stream and along-stream diffusivity in these cells as functions of the sampling interval s . The Davis (1987) diffusivity is shown for comparison; the time lag τ and sampling interval s are shown on a common scale even though the two parameters are not strictly comparable. The MAP diffusivities do demonstrate a degree of convergence at larger sampling intervals, and agree in order of magnitude, at larger sampling intervals, with the large time-lag Davis (1987) diffusivity. The approximate convergence takes place for values of τ and s that are roughly similar and comparable to an estimate of the Lagrangian decorrelation time of the velocity. The MAP diffusivities are never negative, as a consequence of the choice of prior, and while some variation is observed with sampling interval, the Bayesian diffusivity estimates are generally more stable in magnitude than the Davis (1987) diffusivity values.

One of the advantages of the Bayesian approach is that it provides a probability distribution, rather than single estimates for \mathbf{U} and K ,

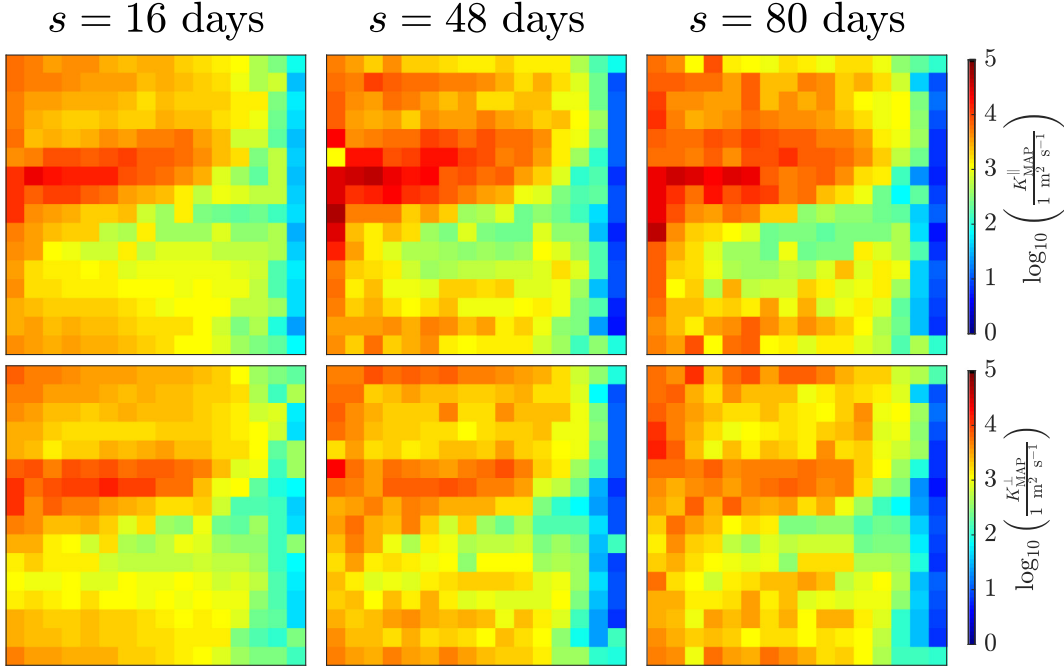


Fig. 7. MAP estimate for the diffusivity components in the middle layer with different sampling intervals. Upper panels: along-stream diffusivity; lower panels: cross-stream diffusivity. A logarithmic colour scale is used.

and hence allows for a quantification of the uncertainty. This is illustrated in Figs. 10 and 11 which also show the (marginal) posterior probability density for the two diffusivity components at each sampling interval s . The probability densities are shown as shading and normalised by their maximum value at each value of s . Broadly speaking, the figures suggest that the range of plausible values is reasonably well constrained, with low probabilities for values more than

a factor of, say 2, away from the MAP. Nevertheless, relatively long tails of the posterior distribution indicate that there is a significant probability of diffusivities of much larger magnitude than the MAP values. There are cases of multi-modality, for example in the middle and top right panel of Figs. 10 and 11, with in this cases a MAP value which switches between the two local maxima. We attribute this to weakness of the flow in these regions which leads to an

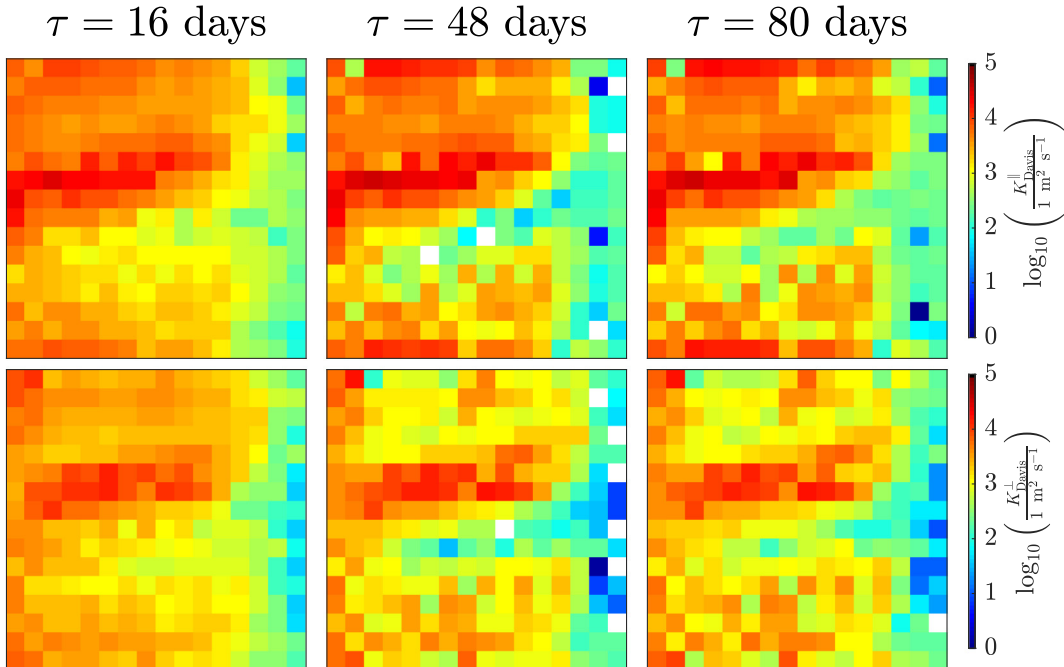


Fig. 8. Davis (1987) diffusivity components in the middle layer with different time lags. Upper panel: along-stream diffusivity; lower panel: cross-stream diffusivity. A logarithmic colour scale is used. Missing data, shown in white, correspond to negative values of the Davis (1987) diffusivity components.

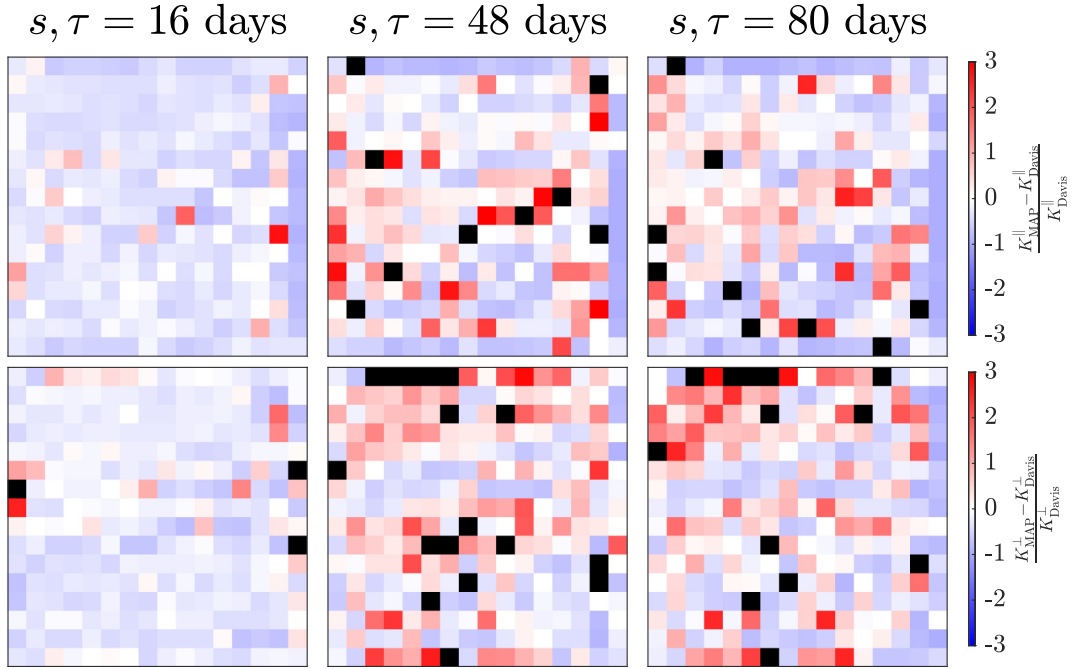


Fig. 9. Relative difference between Davis (1987) and MAP estimates of middle layer diffusivity components with different sampling intervals/time lags. Upper panel: along-stream diffusivity; lower panel: cross-stream diffusivity. Missing data, shown in white, correspond to negative values of the Davis (1987) diffusivity. Data with values exceeding the range of visualisations are shown in black.

ambiguity in the flow direction and hence in the decomposition between along-stream and cross-stream diffusivity.

We assessed the robustness of the inference by carrying out computations under different settings. First, we tested the sensitivity to data size by changing the number of particles from 676 to 169 and 2704 while retaining 10 years of data. The results (not shown) indicate that the MAP estimates of both the mean flow and diffusivity is sensitive in cells with weak mean flow and small numbers of start and end positions records when the number of particles decreases from 676 to 169, but they do not change markedly when the number of particles increases from 676 to 2704. As expected, the posterior distributions narrow as the data size increases. With only 169 particles, the distribution is very broad, so that caution should be exercised when interpreting the inferred diffusivity. This reflects a fundamental limitation in the amount of information provided by the data.

Second, we tested the effect of flow strength by analysing the top layer and the bottom layer of the quasigeostrophic simulation, using again the trajectories of 676 particles. In the bottom layer the diffusivity estimates converge in most of the domain but typically for sampling intervals s considerably larger than in the middle layer. This is attributed to long decorrelation times and the weakness of the flow; the latter improves the validity of the locality assumption. In the top layer the particles rapidly escape from any given cell. This makes the validity of the locality assumption questionable there.

Third, we changed the number of cells in which the domain is partitioned from 16×16 to 8×8 and 32×32 cells. For 8×8 cells, the gyres are poorly resolved in the inferred mean flow and the diffusivity values (covering over longer sampling times) are larger. For 32×32 cells, particles escape cells over timescales that are short compared with that required for the diffusivity estimate to converge, violating the locality assumption. Moreover, very few particle start positions are found in some cells due to their small size, in which the posterior is almost entirely determined by the prior. We emphasise that the dependence of the inferred diffusivity on the number of cells

is expected since different cell sizes correspond to different coarse-graining scales.

5. Conclusions and future work

This article introduces the application of Bayesian inference to the diagnosis of eddy diffusivities from Lagrangian trajectory data. Assuming that the trajectories are governed by a stochastic differential equation involving a number of parameters, the Bayesian inference machinery provides an objective way of incorporating all available data so as to yield a full multidimensional posterior probability distribution for the parameters, which quantifies their plausibility. We utilise this to estimate both an anisotropic diffusivity tensor and a linearly varying non-divergent velocity, and to quantify the uncertainty of the estimates.

Note that the posterior distribution has a very specific interpretation: it is a probability density for the parameters, assuming a perfect model, and given the data and prior information. The posterior can exhibit spread due to lack of data, as weighted against the prior, but not due to error in the underlying model. Further, while we may anticipate convergence with increasing particle number or sampling interval, such limits may in practical oceanographic cases not be achievable.

An idealised experiment, consisting of Taylor–Green vortices embedded within a background flow, is considered. Here, with sufficiently long sampling intervals, the inferred diffusivity components agree well with the predictions from homogenisation theory. In a more complex quasigeostrophic model of a three-layer oceanic gyre system, a “local” approach is applied to infer the middle layer mean flows and diffusivities independently in each of 16×16 cells partitioning the domain. The results show that the data of 676 trajectories over 10 years constrain the diffusivity within a factor of about 2 in most of the domain. The values found become relatively insensitive to the sampling time when this exceeds 30 days or so and are roughly comparable to the Davis (1987) diffusivity.

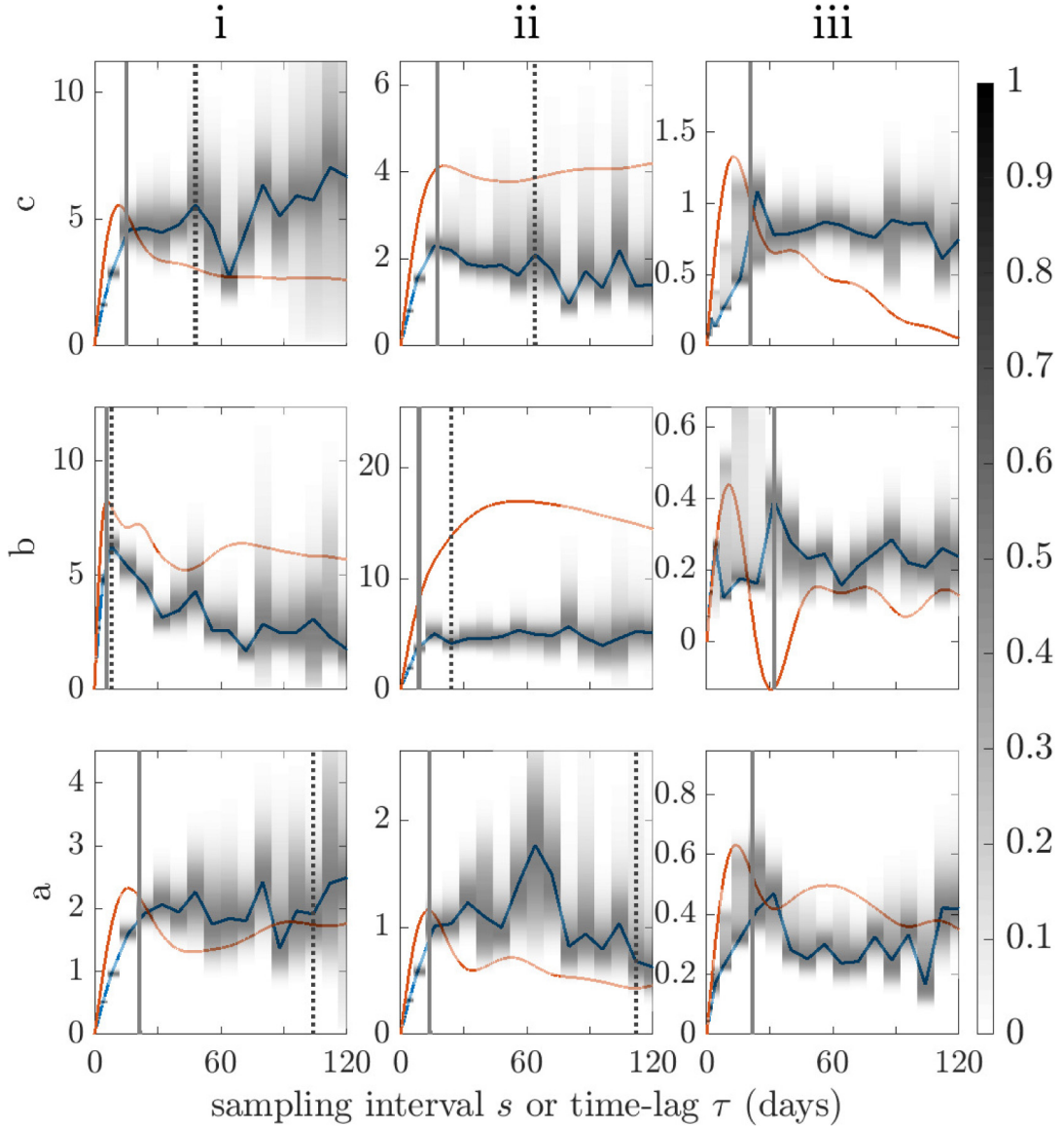


Fig. 10. Cross-stream diffusivity K^L (in $1000\text{m}^2\text{s}^{-1}$) in the middle layer against sampling interval s or time-lag τ in selected cells, labelled on the top of each column and left of each row (see Fig. 2). The blue lines are the MAP estimates of the Bayesian inference; the red lines correspond to the Davis (1987) diffusivity. The grey shading shows the marginal posterior density for K^L , normalised by its maximum values for each s . The dash-dot vertical lines indicate the time taken for 10% of particles to exit the origin and its neighbouring 8 cells. The solid grey vertical lines show the e-folding scale estimated from Lagrangian trajectories as described in Appendix B. Note that the vertical lines are not shown if they correspond to times beyond 128 days.

We emphasise that the Bayesian approach provides a general framework for the inference of diffusivity which extends well beyond the simple implementation presented in this paper. A crucial limitation of this implementation is the assumption of locality, which supposes that particles observed from a given cell are advected by the same flow velocity and experience the same diffusivity over the entire sampling interval. Even with the relatively large size of cells of 240 km, this assumption is problematic, especially near the western boundary and in the region of the separated jet, where the trajectories of many particles straddle several cells. It is hopeless when the cell size is reduced to 120 km. This limitation is however not inherent to the Bayesian framework and can in principle be overcome by considering a discretisation of the velocity and diffusivity over the entire domain, and inferring all associated degrees of freedom simultaneously. Two challenges need to be addressed in this more general case: first, the MCMC sampling of the posterior distribution needs to be performed over a space of much

higher dimension; second, the transition probability, which solves a Fokker–Planck (i.e., advection–diffusion) equation with spatially varying velocity and diffusivity, cannot be evaluated in closed form. The first challenge is not necessarily a major one: theoretical results (Roberts et al., 1997) suggests that the complexity of the simultaneous sampling of all the parameters need not be markedly different from that of the combined sampling of the (independent) parameters associated with a single cell. The second challenge requires efficient methods to compute, likely in an approximated form, the transition probability from the Fokker–Planck equation. This is the subject of ongoing work.

In addition to offering a systematic method to make best use of all available data to estimate diffusivities, the Bayesian approach has the advantage of providing a quantification of the uncertainty of these estimates by means of a complete probability density function. This is important when the amount of data is limited, e.g. for estimates based on real drifters as opposed to simulated trajectories,

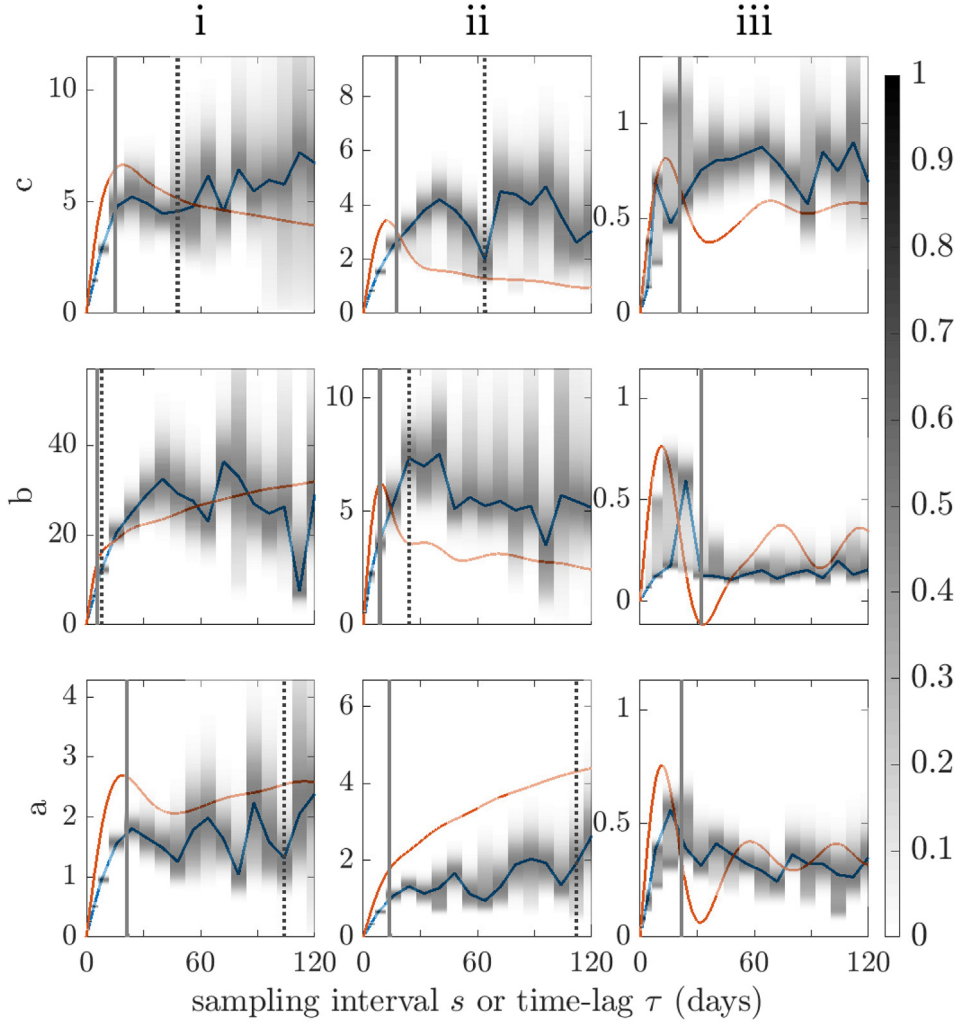


Fig. 11. Same as Fig. 10 but for the along-stream diffusivity K^l in the middle layer.

and could be used prior to measurement campaigns to help assessing how many drifters are needed. Beyond this, we also note that a Bayesian approach can be employed for compressible flow fields, as well as stochastic models of particle motion more sophisticated than Eq. (6) (e.g. Berloff and McWilliams, 2002; Veneziani et al., 2004) and for model selection. This is another direction of future work.

Acknowledgments

YKY was supported by the Principal's Career Development PhD Scholarships and Edinburgh Global Scholarships. YKY acknowledges advice from Alexa Griesel regarding the Davis (1987) diffusivity. The authors are grateful to Luis Zavala Sansón and the anonymous referees for useful comments on the manuscript.

Appendix A. Metropolis–Hastings algorithm

A.1. Algorithm outline

The Metropolis–Hastings Algorithm (e.g. Section 11.2 of Gelman et al., 2013) is outlined as follows.

- Set $k = 0$. Choose a proposal density $P(\cdot|\cdot)$ and take an initial value for the parameter $\theta^{(0)}$.

2. Iterate:

- randomly draw a candidate parameter ϑ with probability $P(\vartheta|\theta^{(k)})$,
- compute $P(\vartheta|\theta^{(k)})$ and $P(\theta^{(k)}|\vartheta)$,
- compute $p(\theta^{(k)}|R)$ and $p(\vartheta|R)$ (up to an irrelevant proportionality constant) from Bayes' formula (9), using the fields $(\mathbf{u}(\mathbf{x}; \theta^{(k)}), K(\mathbf{x}; \theta^{(k)}))$ or $(\mathbf{u}(\mathbf{x}; \vartheta), K(\mathbf{x}; \vartheta))$ for the transition probability π ,
- let

$$\theta^{(k+1)} = \begin{cases} \vartheta & \text{with probability } \alpha, \\ \theta^{(k)} & \text{with probability } 1 - \alpha, \end{cases} \quad (\text{A.1})$$

where

$$\alpha = \min\left(1, \frac{p(\vartheta|R)}{p(\theta^{(k)}|R)} \frac{P(\theta^{(k)}|\vartheta)}{P(\vartheta|\theta^{(k)})}\right), \quad (\text{A.2})$$

- increment $k \mapsto k + 1$.

The proposal density $P(\vartheta|\theta^{(k)})$ should be easy to compute. In this paper, we take it such that all the components of ϑ but one are the same as the components of $\theta^{(k)}$ – a technique known as the

"Gibbs sampler" (Geman and Geman, 1984). Specifically, we take it as the Gaussian

$$P(\boldsymbol{\vartheta}|\boldsymbol{\theta}^{(k)}) = \frac{1}{J} \sum_{j=1}^J \frac{1}{\sqrt{2\pi V_j}} \exp\left(-\frac{(\vartheta_j - \theta_j^{(k)})^2}{2V_j}\right) \prod_{i \neq j} \delta(\theta_i^{(k)} - \vartheta_i), \quad (\text{A.3})$$

where $j = 1, \dots, J$ labels the components of $\boldsymbol{\theta}$ and the variances V_j are tuned for efficient sampling (see below). Note that $P(\boldsymbol{\vartheta}|\boldsymbol{\theta}^{(k)}) = P(\boldsymbol{\theta}^{(k)}|\boldsymbol{\vartheta})$, which simplifies the form of α in Eq. (A.2) and eliminates the need for step 2(b).

It should be noted that it is only the distribution of $\boldsymbol{\theta}^{(k)}$ (the stationary distribution) that converges to the target posterior $p(\boldsymbol{\theta}|R)$. Hence initial samples of the Markov chain should be treated as 'burn-in', that is, only the distribution of $\boldsymbol{\theta}^{(k)}$ for k exceeding a threshold should be considered. In this article, we discard the first half of the $\boldsymbol{\theta}^{(k)}$ for this reason.

To determine the number of MCMC steps needed for the sample distribution of $\boldsymbol{\theta}^{(k)}$ to converge to the target posterior $p(\boldsymbol{\theta}|R)$, the Gelman–Rubin convergence test (Gelman and Rubin, 1992; Brooks and Gelman, 1998, also Section 11.4 of Gelman et al., 2013), which compares multiple chains of $\boldsymbol{\theta}^{(k)}$ under different initial conditions $\boldsymbol{\theta}^{(0)}$, is performed. In this article the convergence of the sample distribution to the target is said to have achieved when \hat{R} (as defined in (11.4) of Gelman et al., 2013) corresponding to each component of $\boldsymbol{\theta}$ falls below 1.2.

A.2. Tuning

To sample the distribution of $p(\boldsymbol{\theta}|R)$ efficiently, the variance of the proposal distribution V_j needs to be tuned. A small variance V_j leads to successive $\boldsymbol{\theta}^{(k)}$ that are very close to one another, while a large V_j leads to numerous rejections; in both cases the support of $p(\boldsymbol{\theta}|R)$ is explored too slowly. For an optimal algorithmic efficiency, a common practice is to maintain the fraction of the candidates $\boldsymbol{\vartheta}$ being accepted to be approximately 0.25 (Roberts et al., 1997). Note that this is measured only after the 'burn-in' phase. A table listing the initial values for the parameter $\boldsymbol{\theta}^{(0)}$ and the proposal standard deviation $\sqrt{V_j}$ (before tuning) is given in Table A.2.

Table A.2

Parameters used to initialise the Metropolis–Hastings Algorithm in the 'burn-in' phase.

Parameter $\boldsymbol{\theta}$	Initial value $\boldsymbol{\theta}^{(0)}$	Proposal standard deviation $\sqrt{V_j}$
U_0	0 m s^{-1}	0.001 m s^{-1}
Φ_0	0 rad	0.05 rad
Υ_1	0 s^{-1}	$2.5 \times 10^{-8} \text{ s}^{-1}$
Υ_2	0 s^{-1}	$2.5 \times 10^{-8} \text{ s}^{-1}$
Φ_A	0 rad	0.05 rad
Γ_1	$1000 \text{ m}^2 \text{ s}^{-1}$	$100 \text{ m}^2 \text{ s}^{-1}$
Γ_2	$500 \text{ m}^2 \text{ s}^{-1}$	$50 \text{ m}^2 \text{ s}^{-1}$
Φ_K	0 rad	0.05 rad

The parameter $\boldsymbol{\theta}_{\text{MAP}}$ that maximises the posterior density $p(\boldsymbol{\theta}|R)$ is used as the initial conditions for tuning V_j and post-'burn-in' sampling. To tune V_j , the algorithm is re-run with an additional 8000 steps, during which the fraction of $\boldsymbol{\theta}^{(k)}$ accepted is recorded. If the acceptance fraction exceeds 0.35, V_j is multiplied by 4/3; if it is lower than 0.15, V_j is multiplied by 2/3. The tuning process is repeated for up to 20 times and stops once the acceptance fraction falls in the range of [0.15, 0.35], in the neighbourhood of the advised value 0.25 (Roberts et al., 1997). With the tuned variance V_j the Metropolis–Hasting algorithm is re-run with initial condition $\boldsymbol{\theta}_{\text{MAP}}$ and the samples of $\boldsymbol{\theta}^{(k)}$ are used for inference.

Appendix B. Calculating the Davis diffusivity

The along-stream and cross-stream Davis (1987) diffusivities are calculated using the 10-year Eulerian mean flow at the centre of each cell to define the mean velocity $\bar{\mathbf{u}}(\mathbf{x})$ appearing in Eq. (4). Evaluating the integral in Eq. (4) requires high temporal resolution; we use particle locations observed every 3 h over 10 years, for 10,000 particles initially deployed uniformly across the domain. We adopt the method of Griesel et al. (2010) to evaluate the two diffusivities in each of the 16×16 cells partitioning the domain. The position of each particle every 3 h is treated as a new independent starting point, to generate a set of particle trajectories each with time lag τ . The conditional averaging operator $\langle \cdot \rangle_{\{\mathbf{X}_i(t)=\mathbf{x}\}}$ in Eq. (4) is then modified to include all particle trajectories that end in a given cell, and the time integral is computed using the trapezoidal rule. Note that, while this formally computes a diffusivity tensor, this tensor need not be symmetric positive definite (or even symmetric) and hence corresponding diffusivity ellipses cannot be shown without further processing. Projecting the diffusivity tensor onto directions parallel to and perpendicular to the Eulerian mean flow yields the along-stream and cross-stream diffusivities shown in Fig. 8.

Appendix C. Estimating an decorrelation timescale

Decorrelation scales of Lagrangian trajectories can be defined using the eddy velocity autocorrelation function

$$R(\mathbf{x}; \tau) = \left\langle \left[\dot{\mathbf{X}}_i(t) - \bar{\mathbf{u}}(\mathbf{x}) \right] \cdot \left[\dot{\mathbf{X}}_i(t + \tau) - \bar{\mathbf{u}}(\mathbf{X}_i(t + \tau)) \right] \right\rangle_{\{\mathbf{X}_i(t)=\mathbf{x}\}}, \quad (\text{C.1})$$

where $\bar{\mathbf{u}}(\mathbf{x})$ is the time-averaged Eulerian mean flow, τ is the time lag and $\langle \cdot \rangle_{\{\mathbf{X}_i(t)=\mathbf{x}\}}$ is the conditional average over particle trajectories that leave position \mathbf{x} at time t . Garraffo et al. (2001) (also appendix of Lumpkin et al., 2002) propose the empirical form

$$R(\mathbf{x}; \tau) = R(\mathbf{x}; 0) \cos\left(\frac{\pi\tau}{2T_z}\right) e^{-(\tau/T_e)^2}, \quad (\text{C.2})$$

with T_z is the first zero crossing time and T_e is an e -folding scale, which we interpret as a decorrelation time – note that the envelope decays more rapidly than exponential. The implementation requires local binning of $\mathbf{X}_i(t)$ and results in an eddy velocity autocorrelation function in each cell. We estimate both parameters T_z and T_e through least-squares fitting.

Appendix D. Parameterisation and solution of linear stochastic differential equations

D.1. Linear velocity parameterisation

A divergence-free linear velocity field $\mathbf{U}(\mathbf{x})$ in Cartesian coordinates can be expressed as

$$\mathbf{U}(\mathbf{x}) = \mathbf{A}(\mathbf{x} - \mathbf{x}_0) + \mathbf{U}_0 \quad (\text{D.1})$$

where $\mathbf{A} = \begin{pmatrix} A_{xx} & A_{xy} \\ A_{yx} & -A_{xx} \end{pmatrix}$ is a constant trace-free velocity-gradient tensor and \mathbf{U}_0 is a constant vector. The velocity gradient tensor \mathbf{A} can be re-expressed in terms of rotationally invariant quantities Υ_1 and Υ_2 via

$$\begin{aligned} \mathbf{A} &= \mathbf{R}(\Phi_A) \begin{pmatrix} 0 & \Upsilon_2 + \Upsilon_1 \\ \Upsilon_2 - \Upsilon_1 & 0 \end{pmatrix} \mathbf{R}(\Phi_A)^T \\ &= \Upsilon_1 \begin{pmatrix} 0 & 1 \\ -1 & 0 \end{pmatrix} + \Upsilon_2 \begin{pmatrix} -\sin 2\Phi_A & \cos 2\Phi_A \\ \cos 2\Phi_A & \sin 2\Phi_A \end{pmatrix}. \end{aligned}$$

with rotation matrix

$$\mathbf{R}(\Phi_A) = \begin{pmatrix} \cos \Phi_A & -\sin \Phi_A \\ \sin \Phi_A & \cos \Phi_A \end{pmatrix}.$$

Υ_1 sets the magnitude of the anti-symmetric part of the velocity gradient tensor and is related to the vorticity via

$$\Upsilon_1 = -\frac{1}{2} \begin{pmatrix} -\partial_y \\ \partial_x \end{pmatrix} \cdot \mathbf{U}(\mathbf{x}) = -\frac{1}{2} \boldsymbol{\omega}.$$

Υ_2 sets the magnitude of the symmetric part of the velocity gradient tensor. If the angle Φ_A is chosen such that Υ_2 is non-negative,

$$\Upsilon_2 = \frac{1}{\sqrt{2}} \|\dot{\varepsilon}\|_F,$$

where $\dot{\varepsilon} = (\nabla \mathbf{U} + (\nabla \mathbf{U})^T)/2$ is the strain rate tensor and $\|\cdot\|_F$ denotes the Frobenius norm.

D.2. Constant diffusivity parameterisation

A constant symmetric diffusivity tensor \mathbf{K} in Cartesian coordinates can be expressed as

$$\mathbf{K} = \begin{pmatrix} K_{xx} & K_{xy} \\ K_{xy} & K_{yy} \end{pmatrix}.$$

The diffusivity tensor \mathbf{K} can be re-expressed in terms of rotationally invariant eigenvalues Γ_1 and Γ_2 via

$$\begin{aligned} \mathbf{K} &= \mathbf{R}(\Phi_K) \begin{pmatrix} \Gamma_1 & 0 \\ 0 & \Gamma_2 \end{pmatrix} \mathbf{R}(\Phi_K)^T \\ &= \frac{\Gamma_1 + \Gamma_2}{2} \begin{pmatrix} 1 & 0 \\ 0 & 1 \end{pmatrix} + \frac{\Gamma_1 - \Gamma_2}{2} \begin{pmatrix} \cos 2\Phi_K & \sin 2\Phi_K \\ \sin 2\Phi_K & -\cos 2\Phi_K \end{pmatrix}, \end{aligned}$$

with rotation matrix

$$\mathbf{R}(\Phi_K) = \begin{pmatrix} \cos \Phi_K & -\sin \Phi_K \\ \sin \Phi_K & \cos \Phi_K \end{pmatrix}.$$

For a symmetric positive-definite \mathbf{K} , the level set satisfying the quadratic equation $\mathbf{x}^T \mathbf{K}^{-1} \mathbf{x} = 1$ is the 'diffusivity ellipse' shown (normalised) in Fig. 6. Geometrically, $\sqrt{\Gamma_1}, \sqrt{\Gamma_2}$ are the two radii of this ellipse and Φ_K is the angle the semi-major axis makes with the x -axis.

D.3. Linear stochastic differential equations

The transition density $\pi(\mathbf{x}, t | \mathbf{y})$ associated with the stochastic differential equation

$$d\mathbf{X}(t) = (\mathbf{A}\mathbf{X}(t) + \mathbf{b})dt + \sqrt{2}\mathbf{K}d\mathbf{W}, \quad \mathbf{X}(0) = \mathbf{y}, \quad (\text{D.2})$$

is a Gaussian, because of the linearity of Eq. (D.2), of the form

$$\pi(\mathbf{x}, t | \mathbf{y}) = \frac{1}{2\pi\sqrt{\det \Sigma(t)}} \exp \left(-\frac{1}{2} (\mathbf{x} - \mathbf{m}(t))^T \Sigma(t)^{-1} (\mathbf{x} - \mathbf{m}(t)) \right), \quad (\text{D.3})$$

with mean and covariance

$$\mathbf{m}(t) = \mathbb{E}\mathbf{X}(t) \quad \text{and} \quad \Sigma(t) = \mathbb{E}(\mathbf{X}(t) - \mathbf{m}(t)) \otimes (\mathbf{X}(t) - \mathbf{m}(t)), \quad (\text{D.4})$$

where \mathbb{E} denotes expectation over the Brownian motion \mathbf{W} . Differentiating Eq. (D.4) with respect to time and using Eq. (D.2) yields

$$\frac{d\mathbf{m}(t)}{dt} = \mathbf{A}\mathbf{m}(t) + \mathbf{b}, \quad (\text{D.5a})$$

$$\frac{d\Sigma(t)}{dt} = \mathbf{A}\Sigma(t) + \Sigma(t)\mathbf{A}^T + 2\mathbf{K}, \quad (\text{D.5b})$$

using Ito's formula (e.g. Pavlitos, 2014). Solving and taking the initial conditions $\mathbf{m}(0) = \mathbf{y}$ and $\Sigma(0) = 0$ into account gives

$$\mathbf{m}(t) = e^{\mathbf{At}}\mathbf{y} + \int_0^t e^{\mathbf{A}(t-s)}\mathbf{b}ds, \quad (\text{D.6a})$$

$$\Sigma(t) = 2 \int_0^t e^{\mathbf{A}(t-s)}\mathbf{K}e^{\mathbf{A}^T(t-s)}ds. \quad (\text{D.6b})$$

Eq. (25) is recovered by letting $\mathbf{b} = \mathbf{U}_0 - \mathbf{Ax}_0$ in Eq. (D.6).

Appendix E. Quasi-geostrophic model

Lagrangian particle trajectories in a quasi-geostrophic model are considered in Section 4. The equations and configuration are as in Marshall et al. (2012) and Maddison et al. (2015). The quasi-geostrophic model solves the multi-layer quasi-geostrophic equations (Pedlosky, 1987; Berloff et al., 2007; Karabasov et al., 2009)

$$\partial_t q_i + \nabla \cdot (\mathbf{u}_i q_i) = \nu \nabla^2 \omega_i - r \delta_{i,3} \omega_i + \delta_{i,1} Q_w \quad \text{for } i \in \{1, 2, 3\}. \quad (\text{E.1})$$

Here the layer is indicated by the subscript i , with $i = 1$ corresponding to the upper layer, $i = 2$ the middle layer, and $i = 3$ the bottom layer, with layer thicknesses $H_1 = 0.25$ km, $H_2 = 0.75$ km, and $H_3 = 3$ km respectively. ∇ is the two-dimensional horizontal del operator. q_i is the quasi-geostrophic potential vorticity, ψ_i the streamfunction, $\mathbf{u}_i = (-\partial_y \psi_i, \partial_x \psi_i)^T$ the geostrophic velocity, and $\omega_i = \nabla^2 \psi_i = \psi_i$ the relative vorticity, each for layer i . $\nu = 100 \text{ m}^2 \text{ s}^{-1}$ is a Laplacian viscosity coefficient, and $r = 4 \times 10^{-8} \text{ s}^{-1}$ is a bottom friction inverse time scale. Q_w corresponds to an upper layer wind forcing, and is given by

$$Q_w = \begin{cases} -\frac{2\pi\tau_0}{\rho_0 H_1 L} A \sin\left(\pi \frac{L/2+y_v}{L/2+y_m}\right) & \text{if } y_v < y_m \\ \frac{2\pi\tau_0}{\rho_0 H_1 L} A \sin\left(\pi \frac{y_v-y_m}{L/2-y_m}\right) & \text{otherwise} \end{cases}, \quad (\text{E.2})$$

where $y_v = y - L/2$ and $y_m = B(x - L/2)$, with $A = 0.9$, $B = 0.2$, $\tau_0 = 0.08 \text{ N m}^{-2}$, and with a reference density of $\rho_0 = 1000 \text{ kg m}^{-3}$. The quasi-geostrophic potential vorticity is related to the streamfunction via

$$q_1 = \nabla^2 \psi_1 + \beta y + s_1^+ (\psi_2 - \psi_1), \quad (\text{E.3a})$$

$$q_2 = \nabla^2 \psi_2 + \beta y + s_2^+ (\psi_3 - \psi_2) + s_2^- (\psi_1 - \psi_2), \quad (\text{E.3b})$$

$$q_3 = \nabla^2 \psi_3 + \beta y + s_3^- (\psi_2 - \psi_3). \quad (\text{E.3c})$$

The parameters s_i^\pm are chosen such that $s_1^+ H_1 = s_2^- H_2 = 2.965 \times 10^{-7} \text{ m}^{-1}$ and $s_2^+ H_2 = s_3^- H_3 = 5.603 \times 10^{-7} \text{ m}^{-1}$. The equations are solved in a square domain with side length $L = 3840$ km, and with partial-slip boundary conditions (Haidvogel et al., 1992) $\alpha \nabla^2 \psi_i = -\nabla \psi_i \cdot \hat{\mathbf{n}}$, where $\hat{\mathbf{n}}$ is an outward unit normal on the boundary, and where $1/\alpha = 120$ km is a partial-slip length scale.

References

- Abernathay, R., Ferreira, D., Klocker, A., 2013. Diagnostics of isopycnal mixing in a circumpolar channel. *Ocean Model.* 72, 1–16.
- Alnæs, M.S., Blechta, J., Hake, J., Johansson, A., Kehlet, B., Logg, A., Richardson, C., Ring, J., Rognes, M.E., Wells, G.N., 2015. The FEniCS project version 1.5. *Arch. Numer. Softw.* 3 (100). <https://doi.org/10.11588/ans.2015.100.20553>.
- Arakawa, A., 1966. Computational design for long-term numerical integration of the equations of fluid motion: two-dimensional incompressible flow. Part I. *J. Comput. Phys.* 1 (1), 119–143.
- Argo, 2000. Argo Float Data and Metadata From Global Data Assembly Centre (Argo GDAC). SEANOE.
- Bachman, S., Fox-Kemper, B., 2013. Eddy parameterization challenge suite I: eddy spindown. *Ocean Model.* 64, 12–28.
- Berloff, P., Hogg, A.M.C., Dewar, W., 2007. The turbulent oscillator: a mechanism of low-frequency variability of the wind-driven ocean gyres. *J. Phys. Oceanogr.* 37 (9), 2363–2386.
- Berloff, P.S., McWilliams, J.C., 2002. Material transport in oceanic gyres. Part II: hierarchy of stochastic models. *J. Phys. Oceanogr.* 32 (3), 797–830.
- Brooks, S.P., Gelman, A., 1998. General methods for monitoring convergence of iterative simulations. *J. Comput. Graph. Stat.* 7 (4), 434–455.
- Cotter, C.J., Pavliotis, G.A., 2009. Estimating eddy diffusivities from noisy Lagrangian observations. *Commun. Math. Sci.* 7 (4), 805–838.
- Davis, R.E., 1987. Modeling eddy transport of passive tracers. *J. Mar. Res.* 45 (3), 635–666.
- Davis, R.E., 1991. Observing the general circulation with floats. *Deep Sea Res. A Oceanogr. Res. Pap.* 38, S531–S571.
- Evans, L.C., 2013. An Introduction to Stochastic Differential Equations. Am. Math. Soc.
- Garrallo, Z.D., Mariano, A.J., Griffa, A., Veneziani, C., Chassignet, E.P., 2001. Lagrangian data in a high-resolution numerical simulation of the North Atlantic: I. Comparison son with in situ drifter data. *J. Mar. Syst.* 29 (1), 157–176.
- Gelman, A., Carlin, J.B., Stern, H.S., Dunson, D.B., Vehtari, A., Rubin, D.B., 2013. Bayesian Data Analysis. Third ed., Chapman and Hall/CRC.
- Gelman, A., Rubin, D.B., 1992. Inference from iterative simulation using multiple sequences. *Stat. Sci.* 7 (4), 457–472.
- Geman, S., Geman, D., 1984. Stochastic relaxation, Gibbs distributions, and the Bayesian restoration of images. *IEEE Trans. Pattern Anal. Mach. Intell. PAMI-6* (6), 721–741.
- Griesel, A., Gilje, S.T., Sprintall, J., McClean, J.L., LaCasce, J.H., Maltrud, M.E., 2010. Isopycnal diffusivities in the Antarctic circumpolar current inferred from Lagrangian floats in an eddying model. *J. Geophys. Res. Oceans* 115 (C6).
- Griffa, A., 1996. Applications of stochastic particle models to oceanographic problems. In: Adler, R., Müller, P., Rozovskii, B. (Eds.), *Stochastic Modelling in Physical Oceanography*. Birkhäuser Boston, pp. 113–140.
- Haidvogel, D.B., McWilliams, J., Gent, P.R., 1992. Boundary current separation in a quasigeostrophic, eddy-resolving ocean circulation model. *J. Phys. Oceanogr.* 22 (8), 882–902.
- Hallberg, R., Gnanadesikan, A., 2006. The role of eddies in determining the structure and response of the wind-driven southern hemisphere overturning: results from the Modeling Eddies in the Southern Ocean (MESO) project. *J. Phys. Oceanogr.* 36, 2232–2252.
- Ham, D.A., 2006. On Techniques for Modelling Coastal and Ocean Flow With Unstructured Meshes. Ph.D. thesis. Technische Universiteit Delft.
- Ham, D.A., Pietrzak, J., Stelling, G.S., 2006. A streamline tracking algorithm for semi-Lagrangian advection schemes based on the analytic integration of the velocity field. *J. Comput. Appl. Math.* 192 (1), 168–174.
- Jayne, S.R., Marotzke, J., 2002. The oceanic eddy heat transport. *J. Phys. Oceanogr.* 32 (12), 3328–3345.
- Karabasov, S.A., Berloff, P.S., Goloviznin, V.M., 2009. CABARET in the ocean gyres. *Ocean Model.* 30 (2–3), 155–168.
- Klocker, A., Ferrari, R., LaCasce, J.H., Merrifield, S.T., 2012. Reconciling float-based and tracer-based estimates of lateral diffusivities. *J. Mar. Res.* 70 (4), 569–602.
- Koszalka, I., LaCasce, J.H., Orvik, K.A., 2009. Relative dispersion in the Nordic Seas. *J. Mar. Res.* 67 (4), 411–433.
- LaCasce, J.H., 2008. Statistics from Lagrangian observations. *Prog. Oceanogr.* 77 (1), 1–29.
- Logg, A., Mardal, K., Wells, G.N., 2012. *Automated Solution of Differential Equations by the Finite Element Method*. Springer.
- Lumpkin, R., Eliop, S., 2010. Surface drifter pair spreading in the North Atlantic. *J. Geophys. Res. Oceans* 115 (C12).
- Lumpkin, R., Treguier, A.-M., Speer, K., 2002. Lagrangian eddy scales in the Northern Atlantic Ocean. *J. Phys. Oceanogr.* 32 (9), 2425–2440.
- Maddison, J.R., Marshall, D.P., Shipton, J., 2015. On the dynamical influence of ocean eddy potential vorticity fluxes. *Ocean Model.* 92, 169–182.
- Majda, A.J., Kramer, P.R., 1999. Simplified models for turbulent diffusion: theory, numerical modelling, and physical phenomena. *Phys. Rep.* 314 (4), 237–574.
- Majda, A.J., McLaughlin, R.M., 1993. The effect of mean flows on enhanced diffusivity in transport by incompressible periodic velocity fields. *Stud. Appl. Math.* 89 (3), 245–279.
- Marshall, D.P., Maddison, J.R., Berloff, P.S., 2012. A framework for parameterizing eddy potential vorticity fluxes. *J. Phys. Oceanogr.* 42 (4), 539–557.
- Marshall, J., Radko, T., 2003. Residual-mean solutions for the Antarctic circumpolar current and its associated overturning circulation. *J. Phys. Oceanogr.* 33 (11), 2341–2354.
- Marshall, J., Shuckburgh, E., Jones, H., Hill, C., 2006. Estimates and implications of surface eddy diffusivity in the Southern Ocean derived from tracer transport. *J. Phys. Oceanogr.* 36 (9), 1806–1821.
- Marshall, J., Shutts, G., 1981. A note on rotational and divergent eddy fluxes. *J. Phys. Oceanogr.* 11 (12), 1677–1680.
- Nakamura, N., 1996. Two-dimensional mixing, edge formation, and permeability diagnosed in an area coordinate. *J. Atmos. Sci.* 53 (11), 1524–1537.
- Oh, I.S., Zhurbas, V., Park, W., 2000. Estimating horizontal diffusivity in the East Sea (Sea of Japan) and the northwest Pacific from satellite-tracked drifter data. *J. Geophys. Res. Oceans* 105 (C3), 6483–6492.
- Panourgias, I., Maddison, J.R., 2016. Parallel supermeshing for multimesh modelling. Tech. Rep., <https://doi.org/10.5281/zenodo.1316942>.
- Pasquero, C., Bracco, A., Provenzale, A., Weiss, J.B., 2007. Particle motion in a sea of eddies. In: Griffa, A., Kirwan, A.D., Jr., Mariano, A.J., Özgökmen, T., Rossby, H.T. (Eds.), *Lagrangian Analysis and Prediction of Coastal and Ocean Dynamics*. Cambridge University Press., pp. 89–118.
- Pavliotis, G.A., 2014. *Stochastic Processes and Applications: Diffusion Processes, the Fokker-Planck and Langevin Equations*. Texts in Applied Mathematics Springer-Verlag New York.
- Pavliotis, G.A., Stuart, A.M., 2007. Parameter estimation for multiscale diffusions. *J. Stat. Phys.* 127 (4), 741–781.
- Pavliotis, G.A., Stuart, A.M., 2008. *Multiscale Methods: Averaging and Homogenization*. Texts in Applied Mathematics Springer-Verlag New York,
- Pedlosky, J., 1987. *Geophysical Fluid Dynamics*. 2nd ed., Springer-Verlag.
- Roberts, G.O., Gelman, A., Gilks, W.R., 1997. Weak convergence and optimal scaling of random walk Metropolis-Hastings algorithms. *Ann. Appl. Probab.* 7 (1), 110–120.
- Rühs, S., Zhurbas, V., Koszalka, I.M., Durgadoo, J.V., Biastoch, A., 2018. Eddy Diffusivity Estimates from Lagrangian trajectories simulated with ocean models and surface drifter data—a case study for the greater Agulhas system. *J. Phys. Oceanogr.* 48 (1), 175–196.
- Rypina, I.I., Kamenkovich, I., Berloff, P., Pratt, L.J., 2012. Eddy-induced particle dispersion in the near-surface North Atlantic. *J. Phys. Oceanogr.* 42 (12), 2206–2228.
- Sallée, J.B., Speer, K., Morrow, R., Lumpkin, R., 2008. An estimate of Lagrangian eddy statistics and diffusion in the mixed layer of the Southern Ocean. *J. Mar. Res.* 66 (4), 441–463.
- Samet, H., 1984. The quadtree and related hierarchical data structures. *ACM Comput. Surv. (CSUR)* 16 (2), 187–260.
- Strang, G., 1986. *Introduction to Applied Mathematics*. Wellesley-Cambridge Press.
- Taylor, G.I., 1922. Diffusion by continuous movements. *Proc. Lond. Math. Soc.* s2-20 (1), 196–212.
- van Sebille, E., Griffies, S.M., Abernathey, R., Adams, T.P., Berloff, P., Biastoch, A., Blanke, B., Chassignet, E.P., Cheng, Y., Cotter, C.J., Deleersnijder, E., Döös, K., Drake, H.F., Drijfhout, S., Garry, S.F., Heemink, A.W., Kjellsson, J., Koszalka, I.M., Lange, M., Lique, C., MacGilchrist, G.A., Marsh, R., Adame, C.G.M., McAdam, R., Nencioli, F., Paris, C.B., Piggott, M.D., Polton, J.A., Rühs, S., Shah, S.H.A.M., Thomas, M.D., Wang, J., Wolfram, P.J., Zanna, L., Zika, J.D., 2018. *Lagrangian ocean analysis: fundamentals and practices*. *Ocean Model.* 121, 49–75.
- Veneziani, M., Griffa, A., Reynolds, A.M., Mariano, A.J., 2004. Oceanic turbulence and stochastic models from subsurface Lagrangian data for the northwest Atlantic Ocean. *J. Phys. Oceanogr.* 34, 1884–1906.